Atomic-orbital-dependent photoelectron momentum distributions for F^- ions by orthogonal two-color laser fields

Jian-Hong Chen,[1,2,*] Meng Han,[2] Xiang-Ru Xiao,[2] Liang-You Peng,[2,3] and Yunquan Liu[2,3,4]

[1]*School of Electronic and Information Engineering, Lanzhou City University, Lanzhou 730070, China*

[2]*School of Physics and State Key Laboratory for Mesoscopic Physics, Peking University, Beijing 100871, China*

[3]*Collaborative Innovation Center of Quantum Matter, Beijing 100871, China*

[4]*Center for Applied Physics and Technology, HEDPS, Peking University, Beijing 100871, China*

(Received 24 July 2018; published 5 September 2018)

We theoretically investigate the two-dimensional photoelectron momentum distributions (PMDs) of F^- ions in an orthogonal two-color laser field with equal intensities. The PMDs for different atomic orbitals are simulated by an exact solution to the three-dimensional time-dependent Schrödinger equation and the strong-field approximation method, respectively. Through the comparison of the calculations of these methods, we confirm that the asymptotic behavior of initial bound-state wave function plays a crucial role in forming the main shape of PMDs at large momenta. Based on the saddle-point method and the imaginary time theory, we show that the PMDs of F^- ions can be decoded to reveal the definite imprint of the photoelectron sub-barrier phase from the subcycle interference structures. We demonstrate the sub-barrier phases from different atomic orbitals have different impacts on the subcycle interference structures.

DOI: 10.1103/PhysRevA.98.033403

I. INTRODUCTION

Photoelectron momentum distributions (PMDs) of atoms and negative ions in strong laser fields have been widely studied in the past decades [1–24]. It has been known that negative ions play an important role in a number of branches of physics, such as plasma physics, astrophysics, atmospheric physics, and accelerator physics [25,26]. With the rapid advancements in photoelectron imaging spectroscopy, a series of consequent measurements about angle-resolved electron spectra for H^- ions and F^- ions have been completed by Kiyan *et al.* [6–12]. For negative ions, the outer electron is bound by short-range polarization forces and the long-range Coulomb effect is absent [25,26]. Therefore, the strong-field approximation (SFA) model, which ignores the Coulomb force after the ionization, is widely used for studying the photodetachment of negative ions in various strong-field schemes [6–24]. As far as we know, for the SFA model of F^- ions, the radial wave function of initial state can be given by the asymptotic wave function [13,24] or the Hartree-Fock–type wave function [10,27].

Alternatively, within the imaginary time theory, the imaginary part of the sub-barrier action is related to the ionization probability [28–30], and the real part of the sub-barrier action is the accumulated sub-barrier phase when electrons tunnel through the potential. In the comparable-intensity orthogonal two-color (OTC) laser fields, the effect of the sub-barrier phase on the interferograms can be amplified and mapped into the two-dimensional polarization plane [31]. In fact, the PMD of negative ions is an ideal platform to reveal the sub-barrier phase because of the short-range potential.

On the other hand, recently, the effect of atomic orbitals with different magnetic quantum numbers on the PMD has been studied experimentally and theoretically [32–36]. The most recent experiment has verified that the photoelectrons with an extremely high degree of spin polarization can be produced in strong-field ionization processes by circularly polarized ultraviolet fields [36].In addition, Shafir *et al.* have demonstrated that each of the three orthogonal $2p$ states (i.e., $2p_x$, $2p_y$, and $2p_z$) of Ne atoms could be selected and individually imaged in the OTC scheme [37]. However, the effect of different initial atomic orbitals on the sub-barrier phase and the photoelectron momentum distributions is rarely investigated.

In this paper, based on the numerical calculations from the three-dimensional time-dependent Schrödinger equation (TDSE) and the SFA model, we show the two-dimensional PMDs of F^- ions for different initial states by an OTC laser pulse. By comparing the TDSE results, the PMDs from the SFA model with the asymptotic wave function, and the PMDs from the SFA model with Hartree-Fock–type wave function, we confirm that the asymptotic behavior of the initial bound-state wave function is crucial for the formation of the main shape of the PMDs of F^- ions in the OTC laser field. Furthermore, based on the saddle-point (SP) method and the imaginary time theory, we demonstrate that the two-dimensional PMDs of F^- ions can be decoded to reveal the definite imprint of the sub-barrier phase on the subcycle interference structures. The effect of the sub-barrier phase on the subcycle interference structures strongly depends on the atomic orbital. Atomic units are used in this paper unless stated otherwise.

*chenyuwen1982@163.com

II. THEORETICAL METHODS

A. SFA model

In the SFA model without considering the rescattering mechanism, the transition probability amplitude from the atomic or ionic ground state $|\psi_{lm}\rangle$ to the continuum state $|\psi_{\mathbf{k}}\rangle$ with momentum $\mathbf{k}$ is given by [12]

$$M_{lm}(\mathbf{k}) = -i\int_{-\infty}^{+\infty}\langle\psi_{\mathbf{k}}|H_i(t)|\psi_{lm}\rangle dt, \tag{1}$$

where $H_i(t) = \mathbf{r}\cdot\mathbf{E}(t)$ is the electron-laser interaction in the length gauge, and $\mathbf{E}(t)$ is the electric field of the laser pulse. l and m are orbital and magnetic quantum numbers of initial state, respectively.

The electric field of the OTC laser pulses with a cosine-square envelope is

$$\mathbf{E}(t) = E_0\cos^2\left(\frac{\pi t}{\tau}\right)[\cos(\omega t)\hat{x} + \cos(2\omega t + \Delta\varphi)\hat{y}] \tag{2}$$

for the time interval $(-\tau/2, \tau/2)$ and zero elsewhere. E_0 is the peak electric field of the laser pulse and ω is the angular frequency of the fundamental laser field. τ is the total duration of the laser pulse and $\Delta\varphi$ is the phase delay between the two colors of OTC pulse. $\hat{x}$ and $\hat{y}$ are the unit polarization vectors of the fundamental field and its second harmonic field, respectively.

The continuum state is, by the Volkov state, approximately

$$\psi_{\mathbf{k}}(\mathbf{r}, t) = \exp\left(i[\mathbf{k} + \mathbf{A}(t)]\cdot\mathbf{r} - \frac{i}{2}\int_{-\infty}^{t}[\mathbf{k} + \mathbf{A}(t')]^2 dt'\right), \tag{3}$$

where $\mathbf{A}(t) = -\int^t \mathbf{E}(t')dt'$ denotes the vector potential of the laser field.

In spherical coordinates, with the z axis as quantization axis, the initial bound-state wave function is given by $\psi_{lm}(\mathbf{r}) = R_{lm}(r)Y_{lm}(\hat{r})$, where the definition of the spherical harmonics $Y_{lm}(\hat{r})$ is same as in Ref. [38]:

$$Y_{lm}(\hat{r}) = Y_{lm}(\Theta,\phi) = \exp(im\phi)\left[\frac{2l+1}{4\pi}\frac{(l-m)!}{(l+m)!}\right]^{1/2} \times P_l^m(\cos\Theta). \tag{4}$$

The radial wave function $R_{lm}(r)$ can be given by asymptotic wave function [13,24] or the Hartree-Fock–type wave function in some other work [10,27]. For the F^- ions with the asymptotic wave function, we have [13,24]

$$R_{lm}(r) = B\frac{\exp(-\kappa r)}{r}, \tag{5}$$

and for the F^- ions with the Hartree-Fock–type wave function, we have [10,27,39]

$$R_{lm}(r) = \sum_i C_i\frac{(2\zeta_i)^{n_i+1/2}}{[(2n_i)!]^{1/2}}r^{n_i-1}\exp(-\zeta_i r), \tag{6}$$

where $\kappa = \sqrt{2I_p}$; $I_p = 3.4$ eV is the ionization potential of the F^- ion. $B = 0.7$ is the asymptotic constant. n_i, l, and m represent principal quantum number, orbital quantum number, and magnetic quantum number, respectively. For F^- ions, the sum of Eq. (6) involves four $2p$ orbitals and the parameters are given as $n_i = 2$, $l = 1$, $C_1 = 0.4704$, $C_2 = 0.3084$, $C_3 = 0.0988$, $C_4 = 0.2470$, $\zeta_1 = 2.0754$, $\zeta_2 = 3.9334$, $\zeta_3 = 1.4660$, and $\zeta_4 = 0.9568$ [27,39].

Usually, the transition amplitude $M_{lm}(\mathbf{k})$ is obtained by numerically integrating over time. For the F^- ions with the asymptotic wave function of Eq. (5), M_{lm} can also be evaluated using the SP method as follows [24]:

$$M_{1m} = -(2\pi)^{3/2}B\sum_{t_s}(\pm1)Y_{1m}(\hat{q}_s)\frac{\exp[i\Phi(t_s)]}{\sqrt{-i\Phi''(t_s)}}, \tag{7}$$

where (±1) corresponds to $\mathbf{k} + \mathbf{A}(\mathbf{t_s}) \to \pm i\kappa$. $\hat{q}_s$ is the unit vector in the direction of the complex canonical momentum $\mathbf{k} + \mathbf{A}(t_s)$.The saddle point t_s is the root of the saddle-point equation $[\mathbf{k} + \mathbf{A}(t_s)]^2 + 2I_p = 0$. $\Phi(t_s) = -\int_{t_s}^{\infty}\{[\mathbf{k} + \mathbf{A}(t')]^2/2 + I_p\}dt'$ is the classical action and $\Phi''(t_s) = -2\mathbf{E}(t_s)\cdot[\mathbf{k} + \mathbf{A}(t_s)]$ is its second derivative. Based on the imaginary time theory [28–30], the action $\Phi(t_s)$ in Eq. (7) can be separated into two parts; i.e.,

$$\Phi(t_s) = \Phi_{\text{sub}} + \Phi_{\text{re}} = -\int_{t_s}^{t_r}\left\{\frac{[\mathbf{k} + \mathbf{A}(t')]^2}{2} + I_p\right\}dt' - \int_{t_r}^{\infty}\left\{\frac{[\mathbf{k} + \mathbf{A}(t')]^2}{2} + I_p\right\}dt'. \tag{8}$$

The sub-barrier action Φ_{sub} is an integral from the complex saddle-point time t_s down to the real time $t_r = \text{Re}t_s$, while Φ_{re} is an integral along the real axis to the end of the pulse. The mathematical treatment of separating the action $\Phi(t_s)$ leads to an intuitive two-step physical picture. Firstly, an electron tunnels through the barrier of negative ions, and then the electron classically moves toward a detector. Actually, the real part of the sub-barrier action $\text{Re}(\Phi_{\text{sub}})$ is related to a phase shift accumulated under the barrier, and the imaginary part $\text{Im}(\Phi_{\text{sub}})$ is related to the ionization rate [28–30]. In this work, we are interested in the effect of sub-barrier phase $\text{Re}(\Phi_{\text{sub}})$ on the PMD.

Note that Eq. (7) not only has validity for the case of a linearly polarized pulse in Ref. [24], but also for the case of the OTC field discussed here. However, the mathematical treatments for $Y_{lm}(\hat{q}_s)$ are different for different schemes. To study the effect of the orbital orientation on the PMD, we choose the orthogonal orbitals $2p_x$ and $2p_y$ as the initial states for F^- ions, respectively. In this paper, we are only interested in the PMDs in the polarization plane of the OTC driving fields. We neglect the $2p_z$ orbital with the polar axis perpendicular to the polarization plane of the laser pulse. The angular components of the $2p_x$ and $2p_y$ orbitals can be respectively defined as linear combinations of the spherical harmonics as follows:

$$\psi_{2p_x}(\hat{r}) = \frac{Y_{1-1}(\hat{r}) - Y_{11}(\hat{r})}{\sqrt{2}}, \tag{9}$$

$$\psi_{2p_y}(\hat{r}) = \frac{i[Y_{11}(\hat{r}) + Y_{1-1}(\hat{r})]}{\sqrt{2}}. \tag{10}$$

Therefore, for the initial states with the $2p_x$ and $2p_y$ orbitals, the transition probability amplitude Eq. (7) can be respectively rewritten as follows:

$$M_{2p_x}(\mathbf{k}) = -4\pi^{3/2}B\sum_{t_s}\frac{k_x + A_x(t_s)}{i\kappa}\frac{\exp\left[i\Phi(t_s)\right]}{\sqrt{-i\Phi''(t_s)}}, \quad (11)$$

$$M_{2p_y}(\mathbf{k}) = -4\pi^{3/2}B\sum_{t_s}\frac{k_y + A_y(t_s)}{i\kappa}\frac{\exp\left[i\Phi(t_s)\right]}{\sqrt{-i\Phi''(t_s)}}. \quad (12)$$

Here k_x, k_y and A_x, A_y represent the final momenta and vector potentials, along the polarization directions of the fundamental field and the second harmonic field, respectively. The two-dimensional PMDs for the orbitals $2p_x$ and $2p_y$ are given by $|M_{2p_x}(\mathbf{k})|^2$ and $|M_{2p_y}(\mathbf{k})|^2$, respectively.

B. TDSE method

The details about the TDSE used in this paper can be found in previous work [40–43]. Here we only briefly introduce the method. Within the single active electron approximation, the time-dependent Schrödinger equation for an atom or a negative ion can be written as

$$i\frac{\partial}{\partial t}\psi(\mathbf{r},t) = [H_0(\mathbf{r}) + H_I(\mathbf{r},t)]\psi(\mathbf{r},t), \quad (13)$$

where $H_0 = -1/2\nabla^2 + V(r)$ is the Hamiltonian of the stationary Schrödinger equation. For the F^- ions, we use the double Yukawa potential as follows:

$$V(r) = -a_1\frac{e^{-a_2 r}}{r} - a_3\frac{e^{-a_4 r}}{r}, \quad (14)$$

where $a_1 = 5.137$, $a_2 = 1.288$, $a_3 = 3.863$, and $a_4 = 3.545$ [21]. The above model potential can give the correct ground-state energy $I_p = 3.4$ eV [21]. The laser-atom interaction is described by the term $H_I(\mathbf{r},t)$ in Eq. (13), whose expression may be given in either the length gauge or the velocity gauge. We adopt the velocity gauge to describe the laser-atom interaction in the present work, but we find that the results for the two gauges agree well. Equation (13) is solved numerically in spherical coordinates and the Crank-Nicolson method is used to propagate the wave function after the operator splitting. The ground-state wave function can be calculated by solving the stationary Schrödinger equation in imaginary time as a diffusion equation for an arbitrary initial trial wave function. In the calculations presented below, the converged TDSE results are obtained by setting $r_{\max} = 3600$ a.u., the radial grid spacing $dr = 0.05$ a.u., the time step $dt = 0.05$ a.u., and the maximum number of partial waves $l_{\max} = 50$.

III. NUMERICAL RESULTS AND DISCUSSION

In this paper, we study the two-dimensional PMDs of F^- ions in a few-cycle OTC laser field by the TDSE and the SFA methods. The OTC field is synthesized by a three-cycle linearly polarized laser pulse at 1400 nm along the x axis and

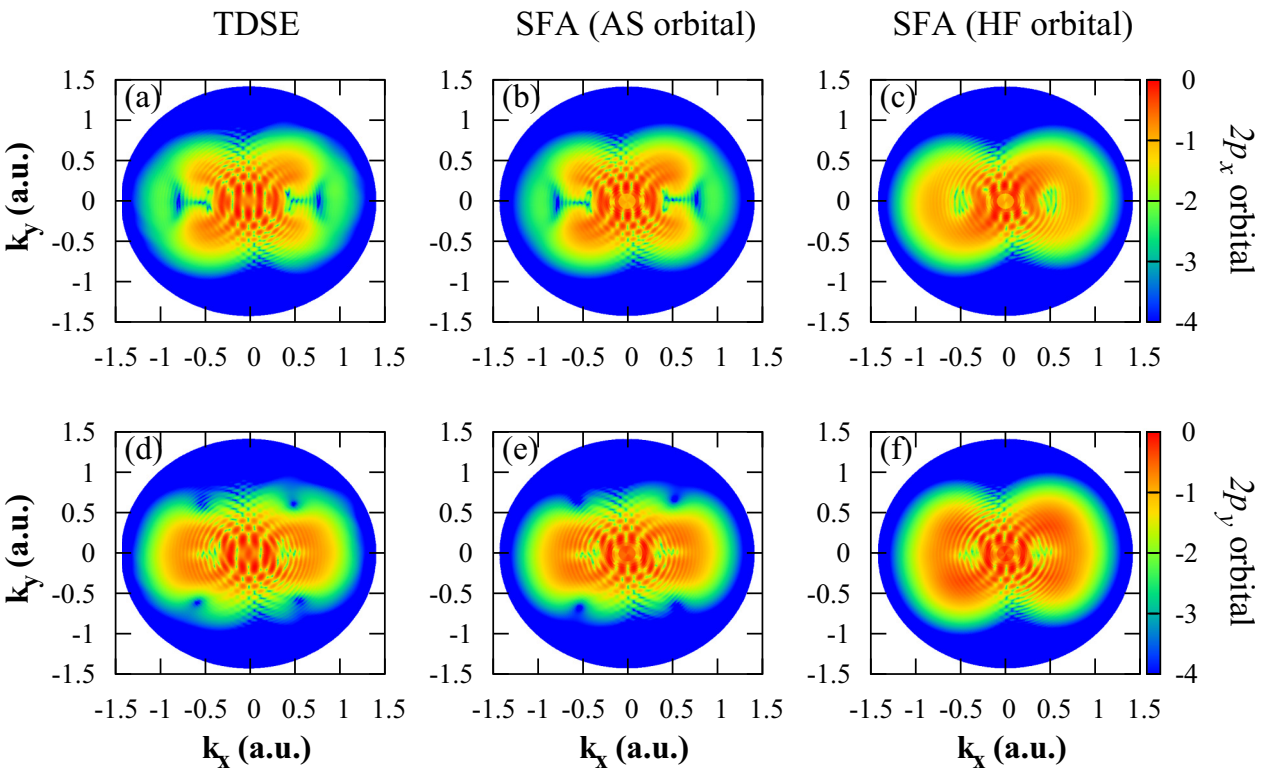

FIG. 1. The two-dimensional photoelectron momentum distributions of F^- ions in the polarization plane of a few-cycle OTC laser field with $\Delta\varphi = 0$, for the $2p_x$ and $2p_y$ orbitals, respectively. The values in the first column are calculated by the TDSE method. The values in the second column are calculated by the SFA method with the asymptotic wave function, and are shown as the AS orbital on the top. The values in the third column are calculated by the SFA method with the Hatree-Fock–type wave function, and are shown as the HF orbital on the top. The data are normalized to the maximum probability and the color is plotted on the logarithmic scale.

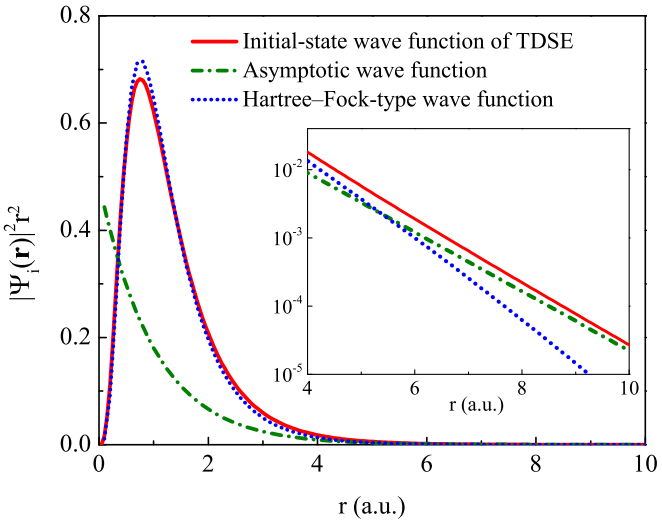

FIG. 2. The radial probability density distributions of the initial-state wave functions used in this work. The solid red line corresponds to the initial-state wave function of the TDSE, which is obtained by solving the stationary Schrödinger equation with the double Yukawa potential in Ref. [21]. The dot-dashed olive line corresponds to the asymptotic wave function of Eq. (5). The dotted blue line corresponds to the Hartree-Fock–type wave function of Eq. (6).

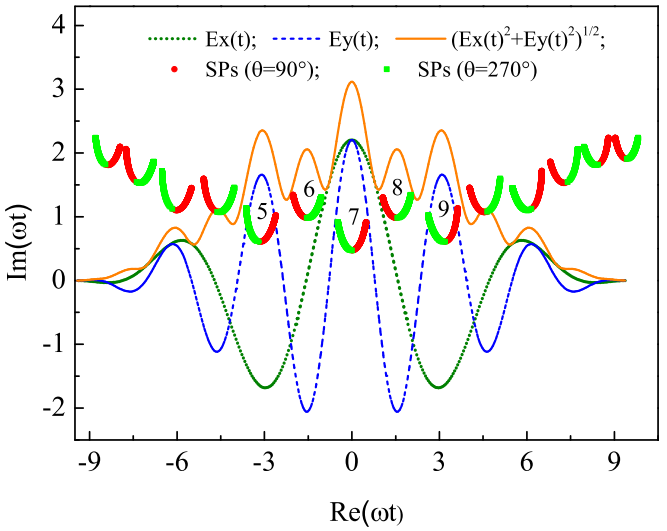

FIG. 3. The temporal sketch of the three-cycle OTC field with $\Delta\varphi = 0$ and the corresponding saddle-point distributions. The dotted olive line, dashed blue line, and solid orange line represent the magnitude of the fundamental field, the second harmonic field, and the synthesized electric field, respectively. Each group of points represents the positions of saddle points for a range of photoelectron energies from 0 to 1.0 a.u. and ejection angles $\theta = 90^\circ$ and $\theta = 270^\circ$. The red (dark gray) points and green (light gray) points indicate the SPs for $\theta = 90^\circ$ and $\theta = 270^\circ$, respectively. The numbers of several dominant SPs are also marked in the complex-time plane.

the second harmonic (700 nm) laser pulse along the y axis. Both the intensities of the fundamental field and the second harmonic field are fixed at $1.7 \times 10^{13}\,\mathrm{W/cm^2}$.

First, we test the validity of the SFA method by comparing with the two-dimensional PMDs from the three-dimensional TDSE calculation. In Fig. 1, we present the two-dimensional PMDs of the F^- ions in the few-cycle OTC field with $\Delta\varphi = 0$. The SFA results are calculated by numerically integrating over time based on Eq. (1). In Figs. 1(b) and 1(e), the asymptotic wave functions [i.e., Eq. (5)] are chosen as the initial state of the SFA method, respectively. By comparing Figs. 1(a) and 1(b) with Figs. 1(d) and 1(e), one can clearly see that the two-dimensional PMDs calculated by the SFA method and by the TDSE agree very well with each other. In addition, the most striking feature in Figs. 1(a) and 1(d) shows that the main shape of the two-dimensional PMDs strongly depend on the atomic orbitals. For the $2p_x$ orbital, a typical ∞-shaped structure is shown in the two-dimensional PMDs [Fig. 1(a)], but for the $2p_y$ orbital, a special structure with four minima on the edge of the two-dimensional PMDs is present in Fig. 1(d). Further careful inspection shows that the number of interference fringes near the center of Fig. 1(a) is different from that of Fig. 1(d). There are three interference fringes along the k_y axis near the center of Fig. 1(a) while two interference fringes along the k_y axis appear near the center of Fig. 1(d). It indicates that the atomic orbital also affects the interference patterns of the two-dimensional PMDs.

In Figs. 1(c) and 1(f), we show the PMDs obtained from the SFA method by choosing the Hartree-Fock–type radial wave function [i.e., Eq. (6)] as the initial state, respectively. By comparing Figs. 1(a) and 1(d) with Figs. 1(c) and 1(f), it is found that the SFA results with Hartree-Fock–type wave function cannot reproduce the TDSE results at large momenta. However, the number of interference fringes near the center of Fig. 1(c) is the same as that of Fig. 1(a), while the number of interference fringes near the center of Fig. 1(f) is the same as that of Fig. 1(d). It suggests that, at the lower momenta, the dependence of interference patterns on the orbital is not changed when we use the Hartree-Fock–type wave function.

We now turn to discuss the reason why the SFA results with Hartree-Fock–type wave function cannot reproduce the TDSE results. In Fig. 2, we give the probability density distributions of three initial wave functions used above. We take the initial wave function obtained from the TDSE as the benchmark result, and compare the results from Eq. (5) with those from Eq. (6). It is found that the Hartree-Fock–type wave function of Eq. (6) is in good agreement with those from the benchmark result when the radius r is less than 4 a.u., but the asymptotic wave function of Eq. (5) is in good agreement with the benchmark result when the radius r is larger than 4 a.u. It suggests that only the asymptotic wave function of Eq. (5) can provide the same asymptotic behavior as the benchmark result. Actually, the results in Fig. 2 are consistent with those in Fig. 1 of Ref. [27]. It has been predicted that the asymptotic behavior of the initial bound-state wave function has an important influence on the multiphoton detachment of negative ions [13]. From Figs. 1 and 2, it can be clearly confirmed that the asymptotic behavior of the initial bound-state wave function plays a dominant role in forming the main shape of the PMDs of F^- ions in the OTC laser field.

In the following, we investigate the effect of sub-barrier phase on the PMDs of the F^- ions in the few-cycle OTC laser field, based on the SP method [3,24,44]. All the exact saddle points can be obtained by solving the saddle-point

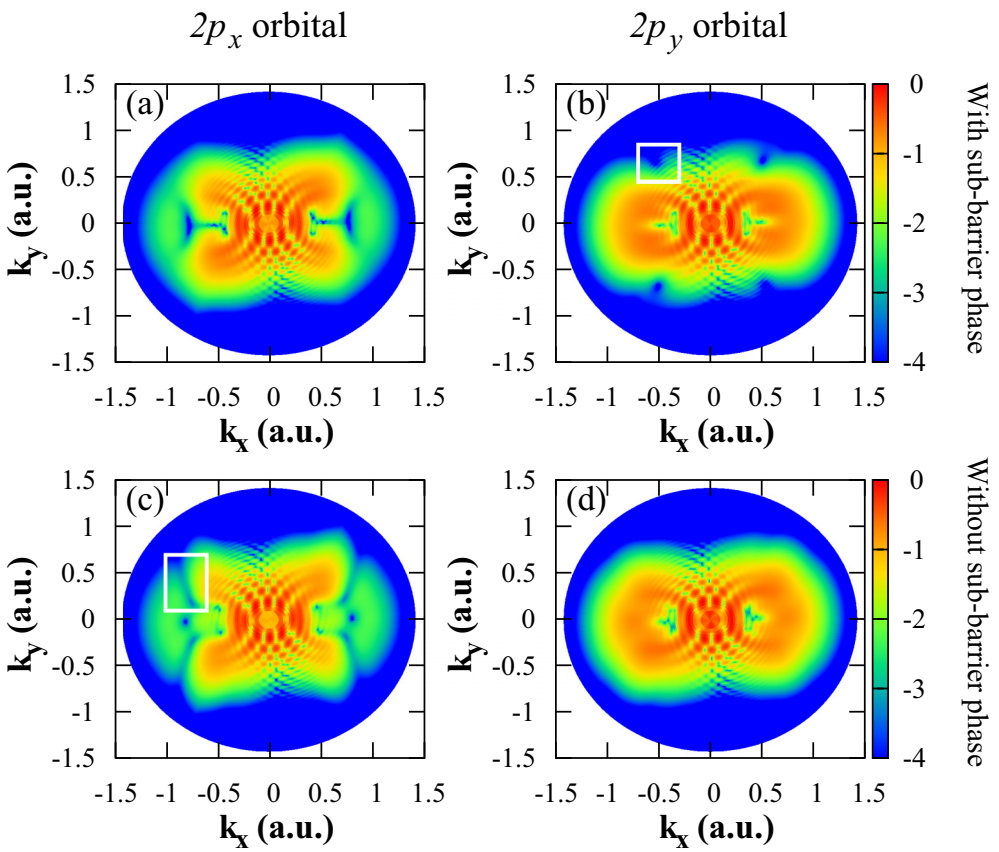

FIG. 4. The PMDs obtained from the SP method by considering five dominant SPs (SPs 5–9), with and without sub-barrier phase, respectively. The values in the first column are the results for the $2p_x$ orbital, and the values in the second column are those for the $2p_y$ orbital. The values in the first row are calculated with the sub-barrier phase. The values in the second row are calculated without the sub-barrier phase. The white rectangle in (b) marks one of the four minima on the edge of the two-dimensional PMDs for the $2p_y$ orbital. The white rectangle in (c) marks one of the four minima in the PMDs for the $2p_x$ orbital when the sub-barrier phase is absent.

equation with the secant method [45,46]. Figure 3 shows the electric field of three-cycle OTC laser pulses with $\Delta\varphi = 0$ and the corresponding SP distributions in the upper half plane of complex time for the fixed angles $\theta = 90^\circ$ and $\theta = 270^\circ$. θ is the ejection angle between the direction of the ejected photoelectron and the x axis. In Fig. 3, each group of points depicts the saddle points for the energy from 0 to 1.0 a.u. with a step size of 0.005 a.u. It is found that there are fourteen SPs as the solutions of the saddle-point equation. The five central SPs, i.e., SP5–SP9, are the lowest five SPs in the upper half plane of complex time. In terms of the imaginary time theory [28–30], the real parts of saddle points SPs 5–9 in Fig. 3 represent the moments when the electrons are released more probably. Further inspection shows that the SPs 5, 7, and 9 correspond to both peaks of the fundamental and the second harmonic fields, while the SPs 6 and 8 only correspond to the peaks of the second harmonic field. It suggests that the second harmonic field gives a dominant contribution to SP6 and SP8, while the synthesized field of the fundamental field and the second harmonic field dominates the SPs 5, 7, and 9.

Based on the imaginary time theory described in Sec. II, the action $\Phi(t_s)$ in Eqs. (8) and (9) can be split into two parts, i.e., $\Phi(t_s) = \Phi_{\rm sub} + \Phi_{\rm re}$. The real part of the sub-barrier action $\Phi_{\rm sub}$ is the accumulated sub-barrier phase when electrons tunnel through the potential, and the imaginary part of $\Phi_{\rm sub}$ is related to the ionization probability [28–30]. In Figs. 4(a) and 4(b), we show the two-dimensional PMDs by considering coherent superposition of SPs 5–9 with the sub-barrier phase. The main structures of Figs. 1(a) and 1(d) from the TDSE calculations can be well reproduced by only considering the contribution of the SPs 5–9. Therefore SPs 5–9 dominate the interference patterns of PMDs in the three-cycle OTC laser pulse with $\Delta\varphi = 0$.

In Figs. 4(c) and 4(d), we give the PMDs without the sub-barrier phase. By comparing Figs. 4(c) and 4(d) with Figs. 4(a) and 4(b), we find that the interference structures at larger momenta are greatly changed if the sub-barrier phase is absent. For the $2p_x$ orbital, there are four interference minima at large momenta in the PMDs of Fig. 4(c) (one of them marked by a white rectangle). Interestingly, for the $2p_y$ orbital, the four interference minima on the edge of the two-dimensional PMDs of Fig. 4(b) [one of them marked by a white rectangle in Fig. 4(b)] are smoothed out in Fig. 4(d), when the sub-barrier phase is dropped out. Therefore, the sub-barrier phase leaves clear fingerprints on the interference structures. However, the interference structures at lower momenta are almost independent of the sub-barrier phase.

To further explore the effect of the sub-barrier phase on the shape formation of the PMDs in Fig. 4, it is necessary to distinguish the contributions of the dominant SPs to the

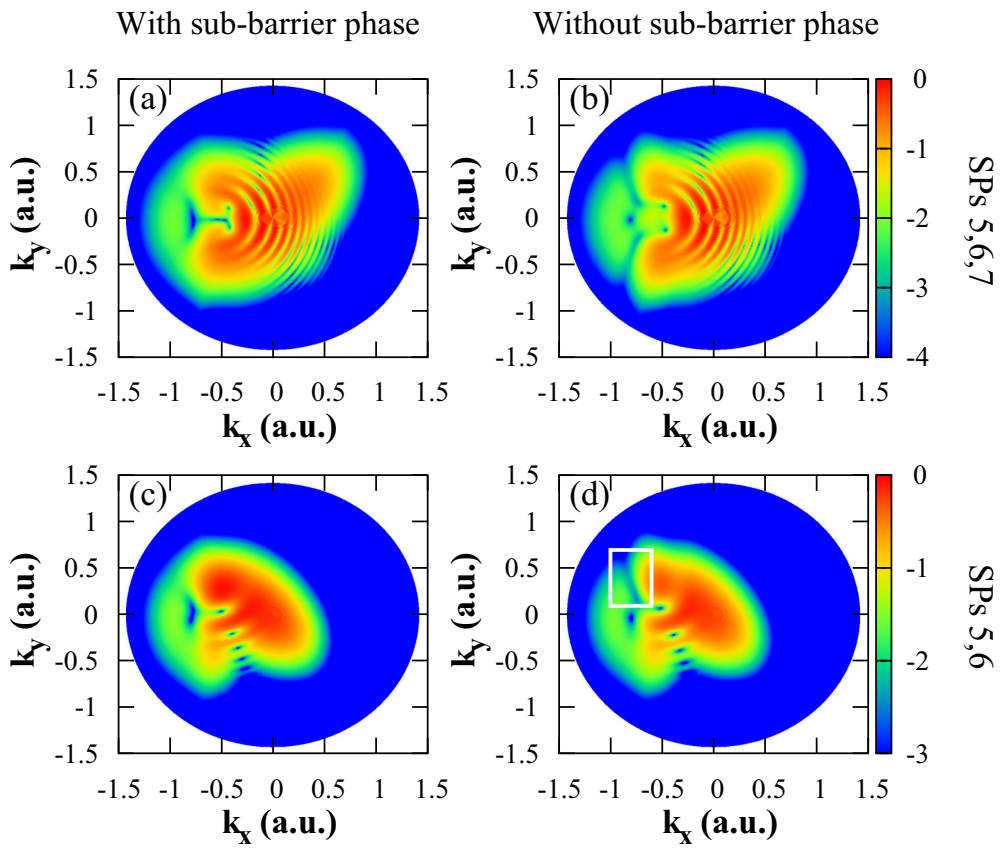

FIG. 5. The PMDs for the $2p_x$ orbital obtained from the SP method with and without sub-barrier phase, by coherently adding different saddle points, respectively. The values in the first row are the results obtained by considering SPs 5–7, and the values in the the second row are obtained by considering SPs 5 and 6. The values in the first column are calculated with the sub-barrier phase. The values in the second column are calculated without the sub-barrier phase. The white rectangle in (d) marks the minima corresponding to those in Fig. 4(c).

interference patterns of the PMDs. Figures 5(a) and 5(b) show the PMDs for the $2p_x$ orbital by coherently adding the contributions of SPs 5–7, with and without sub-barrier phase, respectively. In Figs. 5(a) and 5(b), we can see that the main shape of the PMDs on the left-half plane of Figs. 4(a) and 4(c) can be obtained using only three SPs, i.e., SP5–SP7, except for the absence of the concentric rings centered at zero momentum in Figs. 4(a) and 4(c). As is well known, the intercycle interference arises from the coherent superposition of electron wave packets released at complex times during different optical cycles, whereas subcycle interference comes from the coherent superposition of electron packets released in the same optical cycle [44,47]. In fact, the concentric rings centered at zero momentum in Figs. 1(a) and 4(c) are associated with above-threshold detachment (ATD) rings, which originates from the intercycle interference from wave packets for SP5 and SP9 [45]. Therefore, the interference patterns of Figs. 5(a) and 4(b) on the left-half plane are originated from the subcycle interference from wave packets for SPs 5–7. Figures 5(c) and 5(d) show the PMDs for the $2p_x$ orbital by coherently adding the contributions of SPs 5 and 6, with and without sub-barrier phase, respectively. By comparing Figs. 5(c) and 5(d), it is found that the marked minima in Fig. 4(c) are due to the destructive interference from wave packets for SP5 and SP6, if the sub-barrier phase is dropped in calculations. In fact, we also check the effect of the sub-barrier phase on the other three minima in Fig. 4(c). For example, the minima in the lower-left plane of Fig. 4(c) are due to the destructive interference from wave packets for SP6 and SP7 when the sub-barrier phase is dropped out in calculations.

Figures 6(a) and 6(b) show the PMDs for the $2p_y$ orbital by coherently adding the contributions of SPs 5–7, with and without the sub-barrier phase, respectively. In Figs. 6(a) and 6(b), it is also found that the main shape of the PMDs on the left-half plane of Figs. 4(b) and 4(d) originate from the subcycle interference from wave packets for SPs 5–7. Figures 6(c) and 6(d) show the PMDs for the $2p_y$ orbital by coherently adding the contributions of SPs 5 and 6, with and without the sub-barrier phase, respectively. We can see that the marked minima in Fig. 4(b) are due to the destructive interference from wave packets for SP5 and SP6. In fact, it is found that all four minima in Fig. 4(b) are due to the destructive interference. Therefore, at large momenta, the shape of the interference structure of the PMDs for the both the $2p_x$ and $2p_y$ orbitals highly depends on the sub-barrier phase.

IV. CONCLUSIONS

In summary, we have carried out a systematical analysis on the two-dimensional PMDs of F^- ions in an OTC laser pulse, for the $2p_x$ and $2p_y$ atomic orbitals, respectively. The PMDs obtained from TDSE are regarded as the benchmark results.

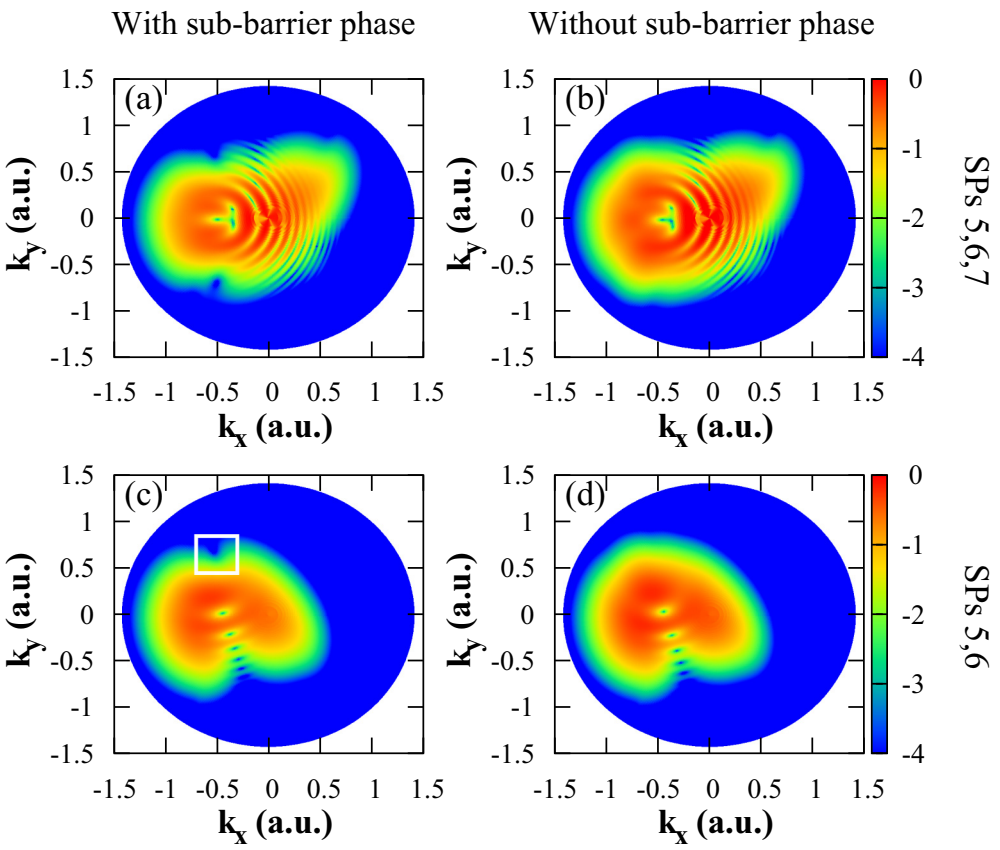

FIG. 6. The same as Fig. 5 but for the $2p_y$ orbital. The white rectangle in (c) marks the minima corresponding to those in Fig. 4(b).

By comparing the TDSE results, the PMDs from the SFA model with the asymptotic wave function, and the PMDs from the SFA model with the Hartree-Fock–type wave function, we find that the interference patterns of the two-dimensional PMDs is strongly dependent on the atomic orbital, and we confirm that the asymptotic behavior of the initial bound-state wave function plays a crucial role in forming the main shape of PMDs at large momenta in the OTC laser field. Moreover, we intuitively reveal that the sub-barrier phase leaves clear fingerprints in the subcycle interference structures, based on the SP method and the imaginary time theory. Specifically, at large momenta, the contribution of the sub-barrier phase will lead to the different subcycle interference structures for different atomic orbitals. The present work provides a deep understanding of the subcycle electron dynamics in the detachment process of negative ions with p-state electrons. We hope the important effects identified in the present work can be experimentally observed in the detachment process of F^- ions with the OTC scheme.

ACKNOWLEDGMENTS

The present work is supported by the National Natural Science Foundation of China (Grants No. 11774013, No. 11647150), the Young Talents Program of Gansu Province (Grant No. 2016-50) in 2016, the Scientific Research Project of Gansu provincial department of education (Grant No. 2016A-068), and the Gansu Provincial Natural Science Foundation of China (Grant No. 18JR3RA230).

[1] P. B. Corkum, Phys. Today **64**(3), 36 (2011).
[2] F. Krausz and M. Ivanov, Rev. Mod. Phys. **81**, 163 (2009).
[3] D. B. Milošević, G. G. Paulus, D. Bauer, and W. Becker, J. Phys. B **39**, R203(R) (2006).
[4] W. Becker, X. Liu, P. J. Ho, and J. H. Eberly, Rev. Mod. Phys. **84**, 1011 (2012).
[5] L. Y. Peng, W. C. Jiang, J. W. Geng, W. H. Xiong, and Q. H. Gong, Phys. Rep. **575**, 1 (2015).
[6] R. Reichle, H. Helm, and I. Y. Kiyan, Phys. Rev. Lett. **87**, 243001 (2001).
[7] R. Reichle, H. Helm, and I. Y. Kiyan, Phys. Rev. A **68**, 063404 (2003).
[8] I. Y. Kiyan and H. Helm, Phys. Rev. Lett. **90**, 183001 (2003).
[9] B. Bergues, Y. Ni, H. Helm, and I. Y. Kiyan, Phys. Rev. Lett. **95**, 263002 (2005).
[10] B. Bergues, Z. Ansari, D. Hanstorp, and I. Y. Kiyan, Phys. Rev. A **75**, 063415 (2007).
[11] B. Bergues and I. Y. Kiyan, Phys. Rev. Lett. **100**, 143004 (2008).

[12] A. Gazibegović-Busuladzić, D. B. Milosević, W. Becker, B. Bergues, H. Hultgren, and I. Y. Kiyan, Phys. Rev. Lett. **104**, 103004 (2010).
[13] G. F. Gribakin and M. Y. Kuchiev, Phys. Rev. A **55**, 3760 (1997).
[14] D. B. Milošević, A. Gazibegović-Busuladžić, and W. Becker, Phys. Rev. A **68**, 050702(R) (2003).
[15] M. V. Frolov, N. L. Manakov, E. A. Pronin, and A. F. Starace, Phys. Rev. Lett. **91**, 053003 (2003).
[16] K. Krajewska, I. I. Fabrikant, and A. F. Starace, Phys. Rev. A **74**, 053407 (2006).
[17] S. Bivona, R. Burlon, and C. Leone, Opt. Express **14**, 12576 (2006).
[18] A. Kramo, E. Hasovic, D. B. Milošević, and W. Becker, Laser Phys. Lett. **4**, 279 (2007).
[19] L. Y. Peng, Q. H. Gong, and A. F. Starace, Phys. Rev. A **77**, 065403 (2008).
[20] M. V. Frolov, N. L. Manakov, and A. F. Starace, Phys. Rev. A **79**, 033406 (2009).
[21] X. X. Zhou, Z. J. Chen, T. Morishita, A.-T. Le, and C. D. Lin, Phys. Rev. A **77**, 053410 (2008).
[22] A. P. Korneev, S. V. Popruzhenko, S. P. Goreslavski, W. Becker, G. G. Paulus, B. Fetić, and D. B. Milošević, New J. Phys. **14**, 055019 (2012).
[23] S. F. C. Shearer and C. R. J. Addis, Phys. Rev. A **85**, 063409 (2012).
[24] S. F. C. Shearer and M. R. Monteith, Phys. Rev. A **88**, 033415 (2013); G. F. Gribakin and S. M. K. Law, *ibid.* **94**, 057401 (2016).
[25] D. J. Pegg, Rep. Prog. Phys. **67**, 857 (2004).
[26] T. Andersen, Phys. Rep. **394**, 157 (2004).
[27] B. Fetić, D. B. Milošević, and W. Becker, J. Mod. Opt. **58**, 1149 (2011).
[28] T. M. Yan and D. Bauer, Phys. Rev. A **86**, 053403 (2012).
[29] V. S. Popov, Phys. At. Nucl. **68**, 686 (2005).
[30] S. V. Popruzhenko, J. Phys. B **47**, 204001 (2014).
[31] M. Han, P. Ge, Y. Shao, M. M. Liu, Y. Deng, C. Wu, Q. Gong, and Y. Liu, Phys. Rev. Lett. **119**, 073201 (2017).
[32] I. Barth and O. Smirnova, Phys. Rev. A **88**, 013401 (2013).
[33] D. B. Milošević, Phys. Rev. A **93**, 051402(R) (2016).
[34] A. Hartung, F. Morales, M. Kunitski, K. Henrichs, A. Laucke, M. Richter, T. Jahnke, A. Kalinin, M. Schöffler, L. Ph. H. Schmidt, M. Ivanov, O. Smirnova, and R. Dörner, Nat. Photonics **10**, 526 (2016).
[35] M.-M. Liu, M. Li, Y. Shao, M. Han, Q. Gong, and Y. Liu, Phys. Rev. A **96**, 043410 (2017).
[36] M.-M. Liu, Y. Shao, M. Han, P. Ge, Y. Deng, C. Wu, Q. Gong, and Y. Liu, Phys. Rev. Lett. **120**, 043201 (2018).
[37] D. Shafir, Y. Mairesse, D. M. Villeneuve, P. B. Corkum, and N. Dudovich, Nat. Phys. **5**, 412 (2009).
[38] D. A. Varshalovich, A. N. Moskalev, and V. K. Khersonskii, *Quantum Theory of Angular Momentum: Irreducible Tensors, Spherical Harmonics, Vector Coupling Coefficients, 3nj symbols* (World Scientific, Singapore, 1988).
[39] A. A. Radzig and B. M. Smirnov, *Reference Data on Atoms, Molecules, and Ions* (Springer-Verlag, Berlin, 1985).
[40] L. Y. Peng, E. A. Pronin, and A. F. Starace, New J. Phys. **10**, 025030 (2008).
[41] M. H. Xu, L. Y. Peng, Z. Zhang, Q. Gong, X. M. Tong, E. A. Pronin, and A. F. Starace, Phys. Rev. Lett. **107**, 183001 (2011).
[42] M. V. Frolov, D. V. Knyazeva, N. L. Manakov, A. M. Popov, O. V. Tikhonova, E. A. Volkova, M. H. Xu, L. Y. Peng, L. W. Pi, and A. F. Starace, Phys. Rev. Lett. **108**, 213002 (2012).
[43] S. N. Song, J. W. Geng, H. B. Jiang, and L. Y. Peng, Phys. Rev. A **89**, 053411 (2014).
[44] D. G. Arbó, S. Nagele, X.-M. Tong, X. Xie, M. Kitzler, and J. Burgdörfer, Phys. Rev. A **89**, 043414 (2014).
[45] J. H. Chen, S. F. Zhao, M. Han, and Y. Q. Liu, Opt. Express **26**, 14086 (2018).
[46] J. H. Chen, S. F. Zhao, G. L. Wang, and X. X. Zhou, J. Phys. B **47**, 245601 (2014).
[47] D. G. Arbó, K. L. Ishikawa, K. Schiessl, E. Persson, and J. Burgdörfer, Phys. Rev. A **81**, 021403 (2010).